Dynamic instability in the hook-flagellum system that triggers bacterial flicks

Mehdi Jabbarzadeh and Henry Chien Fu

Phys. Rev. E **97**, 012402 — Published 11 January 2018

DOI: 10.1103/PhysRevE.97.012402

The dynamic instability in the hook/flagellum system that triggers bacterial flicks

Mehdi Jabbarzadeh and Henry Chien Fu*
Department of Mechanical Engineering, University of Utah, Salt Lake City, UT 84112 USA
(Dated: December 29, 2017)

Dynamical bending, buckling, and polymorphic transformations of the flagellum are known to affect bacterial motility, but run-reverse-flick motility of monotrichous bacteria also involves the even more flexible hook connecting the flagellum to its rotary motor. Although flick initiation has been hypothesized to involve either static Euler buckling or dynamic bending of the hook, the precise mechanism of flick initiation remains unknown. Here, we find that flicks initiate via a dynamic instability requiring flexibility in both the hook and flagellum. We obtain accurate estimates of forces and torques on the hook that suggest that flicks occur for stresses below the (static) Euler buckling criterion, then provide a mechanistic model for flick initiation that requires combined bending of the hook and flagellum. We calculate the triggering torque:stiffness ratio and find that our predicted onset of dynamic instability corresponds well with experimental observations.

I. INTRODUCTION

The deformations of rotating filaments play an important role in bacterial motility. The dynamical bending of rotating rods and helices and its effect on swimming has been extensively investigated[1–6], including in the context of flagellar extension[7–12], polymorphic transitions[11, 13–17], bundling[18–24], and wrapping around the cell body[25]. Dynamical configurations of rotating filaments have also been considered for microrobotic propulsion[26, 27]. Here, we concentrate on monotrichous bacteria such as *Vibrio alginolyticus* that swim by rotating a single helical flagellar filament and display the ubiquitous run-reverse-flick motility[28], in which straight forward and backward runs are interspersed with reorienting flicks caused by deformation of the flagellum up to 90°[29] off-axis.

Rotary motion of the flagellum is driven by a motor embedded in the cell body that is connected to the flagellar filament by a structure called the hook, which plays a crucial role in flicks. The hook is much shorter and more flexible than the flagellum. As thin filaments, their resistance to bending is measured by a bending stiffness (EI, where E is the Young's modulus and I a second moment of the cross-sectional area, see Eq. 1). Hook lengths are $L_H = 100$ nm and bending stiffnesses are $EI \approx 10^{-25}$ Nm^2, while flagellum arclengths are $L \approx 5\mu$m and stiffnesses are $EI \approx 10^{-23}$ Nm^2. The events before and after the flick are summarized in the inset to Fig.1. Key to this paper are the pre-flick forward run (B) in which compressive forces and torques build up to trigger the flick (C), and the post-flick forward run (D) in which the flagellum has returned to an on-axis orientation. The difference between the two is that pre-flick, clockwise rotation during backward swimming (A) unwinds the hook leading to a smaller bending stiffness ($EI_u = 3.6 \pm 0.4 \times 10^{-26}$ Nm^2), while post-flick, counterclockwise rotation winds the hook leading to a larger bending stiffness ($EI_w = 2.2 \pm 0.4 \times 10^{-25}$ Nm^2)[29].

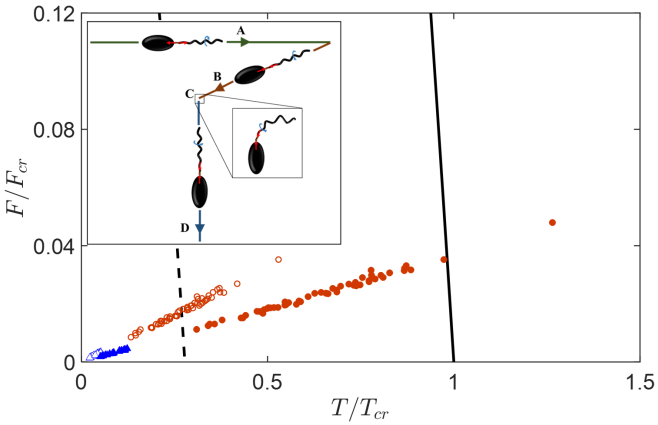

FIG. 1. Inset: After swimming backwards (A) with clockwise flagellar rotation, which unwinds the hook and decreases its stiffness to EI_u, reversal of the flagellar motor leads to a short pre-flick forward run (B) that increases loading on the hook and causes a flick (C) in which the flagellum deforms off-axis and turns the bacteria. Post-flick, the wound hook with increased bending stiffness EI_w returns the flagellum on-axis for a forward run (D). Main figure: axial torques and forces on hook during pre-flick (flick-triggering, red circles, EI_u) and post-flick (non-flick-triggering, blue triangles, EI_w) runs of different bacteria, estimated by Son et al's[29] 1D model (open symbols) and our full hydrodynamic model (filled symbols). Solid line is static Euler buckling criterion, while dashed line is Euler buckling criterion if $EI = 1 \times 10^{-26}$ Nm^2 (see text).

The mechanism triggering flicks remains imprecisely understood. Flicks have been proposed to involve buckling of the hook in static Euler buckling[29]. Buckling of the flagellum during swimming has been investigated[5, 15], but only a few recent studies explicitly consider the role of the hook, and in flicks always in the case of effectively rigid flagellum. For free swimmers, Shum *et al* used a boundary element method to model hydrodynamic interactions of the cell body and a rigid flagellum connected by a hook modeled as an inextensible Kirchoff rod[30]. They did not address flicks and due to computational expense provided detailed results for only a few geome-

* henry.fu@utah.edu

try and hook stiffness scenarios. Modeling the hook as a torsional spring connected to a rigid flagellum, Nguyen *et al*[31] described a transition from straight hook and straight trajectories to bent hook and helical trajectories as hook stiffness decreased. Park *et al*[32] modeled flicks using a time-dependent decrease in hook stiffness and flagellum stiff enough not to bend, but their model could be at most qualitative since the bacteria were not free-swimming. While their model showed off-axis motion, it did not lead to hook bending with deflections more than 25°, and they did not compare predictions for the onset of flick behavior to experimental observations. Flagellar precession due to hook bending has also been observed and modeled for surface-attached bacteria[33].

Here, we combine theoretical modeling with experimental data to determine the mechanism of flick initiation. We show that the flick is triggered by a dynamic buckling requiring both hook and flagellum bending, and find good agreement between predicted torque:stiffness ratios required to trigger flicks and experimental observations. Flicks are a biological example of how failure of compliant structures can be used constructively, a potential design paradigm for soft robotics. For any design application, predictive models yielding quantitative criteria for failure are necessary; our work provides an example of such a predictive model.

A. Critical torques and forces for flick initiation suggest a dynamical, not static, buckling mechanism.

The torque (**M**) and force (**F**) on the hook required to cause flicks provides clues to the mechanism of flick initiation. To quantify the forces and torques needed to initiate flicks, Son *et al.*[29] imaged swimming cell body geometries and velocities[34] during pre-flick as well as post-flick forward runs. They calculated the motor torque and axial hook force using a one-dimensional (1D) model[29] that used the known drag coefficients for ellipsoidal cell bodies with the imaged dimensions, and drag coefficients and rotation-torque coupling coefficients for the flagellum (geometry in Table I) obtained from resistive force theory. Their results are plotted in Fig. 1 (open symbols). In this plot, values are scaled by the critical force $F_{cr} = \pi^2 EI/L_H^2$ and critical torque $M_{cr} = 2\pi EI/L_H$, using the measured[29] bending stiffnesses EI_u for pre-flick runs, and EI_w for post-flick runs. Son *et al.* noted that the average force and torque of pre-flick runs just exceed the Euler buckling criterion $F/F_{cr} + (M/M_{cr})^2 > 1$ if it were calculated using a smaller $EI = 1.0 \times 10^{-26}$ Nm^2 (dashed line in Fig. 1, plotted using EI_u for F_{cr} and T_{cr} in the axes normalization), which is of the same order of magnitude but outside the error of the measured EI_u, and they suggested that the flick initiation is caused by a static Euler buckling of the hook.

We reanalyzed the data from pre- and post-flick runs using our previously described implementation[36–38] of the method of regularized Stokeslets[39, 40]. The method of regularized Stokeslets is a well-established numerical technique that calculates fluid velocity fields, swimming speeds, and trajectories for bacteria; it can handle complex geometries and accounts for all hydrodynamic interactions and is therefore expected to be significantly more accurate[37] than the 1D model. The cell body is modeled as a prolate ellipsoid with major axis $2a$ and minor axis $2b$. The flagellum is modeled as a rigid helical filament with filament radius r, helical radius R, and helical pitch P specified in Table I and a taper that ensures the filament is normal to the cell body at the attachment (see SM[41]). We prescribe a fixed rotation rate for a flagellum orientation along the x-direction for forward runs. For a given body geometry, due to the linearity of Stokes equations the swimming speed, force, and torque on the hook are proportional to the rotation rate (ω) of the flagellum. Therefore, choosing ω to match the swimming speed with its experimental value also determines the force and torque on the hook.

Our results are plotted (filled symbols) in Fig.1. The x-components of forces ($0.4 - 1.7$ pN) and torques ($700 - 2860$ pN nm) are approximately 1.3 and 2.4 times larger than forces ($0.3 - 1.3$ pN) and torques ($300 - 1200$ pN nm) estimated by the 1D model (full results in Table S1). It is evident that the forces and torques are not large enough to exceed the static Euler buckling criterion of the hook (black line). Therefore, in this paper we explore the possibility that the flick mechanism involves dynamical buckling of the hook.

B. Outline.

To investigate the role of hook and flagellar bending in flicks, we first study the response of a hook modeled as an inextensible Kirchoff rod to forces and torques exerted by the cell body and flagellum and show that the response can accurately be linearized (but not as a simple torsional spring) in the biologically relevant regime. Then, we take advantage of the computational advantages of such linearization to explore flagellum orientation dynamics in a model of a swimming bacterium with rigid flagellum connected to the cell body by the linearized hook. As hook stiffness decreases there is a transition from on-axis flagellar rotation to off-axis flagellar precession. However, precession alone cannot explain the large ($> 60°$) flagellar reorientations observed during flicks. We show that precession is not realized since forces during precession lead to the significant flagellar bending seen during flicks, by treating the flagellum as an extensible Kirchoff rod coupled to hydrodynamic forces. Thus, we establish the mechanism by which combined flexibility of hook and flagellum initiate flicks. Finally, we calculate triggering torque:stiffness ratios for different cell sizes and find that the predicted onset of dynamic instability corresponds well with experimental observations.

TABLE I. Dimensions of the flagellar filament and cell body for *V. alginolyticus*. (All values are taken from [29], except values for EA and GA which are taken from [4, 35].)

Flagellar filament								Cell body	
Flagellar pitch	Filament radius	Helix radius	Contour length	Bending stiffness	Torsional stiffness	Stretch stiffness	Shear stiffness	Head length	Head width
P(μm)	r (μm)	R(μm)	L(μm)	EI(Nm^2)	GJ(Nm^2)	EA(N)	GA(N)	$2a$ (μm)	$2b$(μm)
1.49 ± 0.02	0.016	0.14 ± 0.02	4.59 ± 1	10^{-23}	10^{-23}	8×10^{-10}	8×10^{-10}	3.2 ± 0.5	1.2 ± 0.1

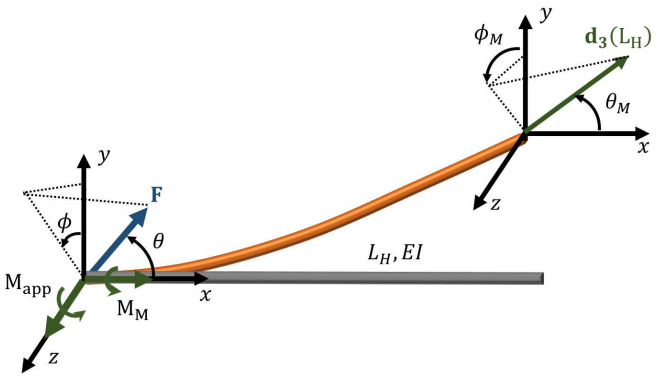

FIG. 2. Forces $\mathbf{F}$, motor (M_M) and perpendicular (M_{app}) torques at one end of a hook deform it from a straight rest position in the x-direction so that the tangent direction at the other end is $\mathbf{d}_3(L_H)$, described by polar angles (θ_M, ϕ_M).

II. METHODS

A. Inextensible Kirchoff rod model of hook.

Since the radius of the hook is only 10 nm, following [30] we treat it as a slender inextensible Kirchoff rod which resists bending due to elastic material response. During motion, hydrodynamic forces and torques arise on the cell body and flagellum, but we ignore hydrodynamic forces on the hook itself due to its short length.

This model is described in detail in [30], but briefly, the undeformed hook of length L_H is straight and in the x-direction (Fig. 2). As a function of the arclength $s \in [0, L_H]$ the position $\mathbf{x}(s)$ defines the deformed centerline of the rod with an associated orthonormal triad $\{\mathbf{d_1}(s), \mathbf{d_2}(s), \mathbf{d_3}(s)\}$. $\mathbf{d_1}(s)$ and $\mathbf{d_2}(s)$ specify the orientations of material cross sections of the rod and $\mathbf{d_3}(s) = \mathbf{d_1}(s) \times \mathbf{d_2}(s) = \partial \mathbf{x}/\partial s$ is tangent to the centerline. At each cross section, a force $\mathbf{F}$ and moment $\mathbf{M}$ are exerted by the material with greater s on the material with lesser s. The constitutive law for the moment is

$$\mathbf{M} = EI(\kappa_1 \mathbf{d}_1 + \kappa_2 \mathbf{d}_2) + GJ\kappa_3 \mathbf{d}_3, \tag{1}$$

where the twist vector $\boldsymbol{\kappa} = \kappa_i(s)\mathbf{d}_i(s)$ measures the local curvature of the rod via $\partial_s \mathbf{d}_i = \boldsymbol{\kappa} \times \mathbf{d}_i$, EI is the bending stiffness related to Young's modulus E, and GJ is the torsional stiffness of the rod related to shear modulus G. I and J are second moments of the cross sectional area about the bending or twisting axis, respectively.

The Kirchhoff equations,

$$\partial_s \mathbf{F} = 0, \qquad \partial_s \mathbf{M} + \mathbf{d}_3 \times \mathbf{F} = 0, \tag{2}$$

express local force and moment balance on rod elements in the absence of external (hydrodynamic) forces and torques, and together with Eq. 1 yield a system of ODEs that can be solved given initial conditions at $s = 0$ (the cell body). Nondimensionalizing to tilde variables by using L_H as the unit of length and EI/L_H^2 as the unit of force, the ODEs are

$$\begin{aligned}
\mathbf{d}_i^{'} &= \tilde{\kappa} \times \mathbf{d}_i, \\
\tilde{\kappa}_1^{'} &= (\tilde{\mathbf{F}} \cdot \mathbf{d}_2) - \tilde{\kappa_2}\tilde{\kappa_3}(\Gamma - 1), \\
\tilde{\kappa}_2^{'} &= -(\tilde{\mathbf{F}} \cdot \mathbf{d}_1) + \tilde{\kappa_1}\tilde{\kappa_3}(\Gamma - 1), \\
\tilde{\kappa}_3^{'} &= 0, \\
\tilde{\mathbf{x}}^{'} &= \mathbf{d}_3.
\end{aligned} \tag{3}$$

where $(\cdot)^{'} = \partial(\cdot)/\partial\tilde{s}$, and $\Gamma = GJ/EI$ is the ratio of the torsional to bending stiffness. We solve these using a fourth order Runge-Kutta scheme.

B. Linearization of hook response.

In the zero-Reynolds-number limit appropriate for bacteria[42], the forces (and torques) exerted by the hook on the flagellum and cell body are equal and opposite. The shape that the hook takes under these applied torques determines the relative orientation of the flagellum and cell body. Equations 3 are solved by imposing boundary conditions at the hook-cell body junction ($s = 0$). The boundary conditions are determined by considering that the flagellar motor keeps the attached end of the hook normal to the cell body surface and applies a nearly constant motor torque[43] in the x-direction. To keep the end of the hook normal to and translating with the cell body, there are also constraint torques in the y- and z directions and constraint forces applied to the hook by the cell body. Thus we study the deformations of the hook while varying the torque $\mathbf{M}_0$ (with motor x-component M_M) and force $\mathbf{F}_0$, defined as applied on the cell body by the hook. The dominant influence of the hook on swimming dynamics is due to change in the orientation of the flagellum relative to the cell body[30];

we ignore displacements of the hook endpoint since it is much shorter than the flagellum or cell body. The orientation of the flagellum is determined by the direction of the hook's end, $\mathbf{d}_3(s = L_H)$.

Without loss of generality, we consider the case where $M_{app} > 0$, the non-motor component of $\mathbf{M}_0$, is in the z-direction (Fig. 2) and calculate $\mathbf{x}(s)$. The orientation of $\mathbf{d}_3(L_H)$ is specified by angles (θ_M, ϕ_M). Dimensional analysis implies that both these angles are functions of $\{GJ/EI, k_H = |EI/L_H M_M|, M_{app}/M_M, \mathbf{F}_0 L_H^2/EI\}$. In Appendix A, we show that the effects of typical $\mathbf{F}_0$ on $\mathbf{d}_3(L_H)$ are $< 4\%$ of the effects of typical $\mathbf{M}_0$. Furthermore, GJ/EI has little influence on swimming dynamics[30] so we always use $GJ = EI$. Thus, we seek to model the orientation of $\mathbf{d}_3$ as a function of only k_H and M_{app}/M_M. For a given k_H, we find that (θ_M, ϕ_M) are well-approximated by linear functions of M_{app}/M_M in much of the regime experienced by *V. alginolyticus* [1000 pN nm $< M_M <$ 4000 pN nm[44], $0.1 < k_H < 2$[29], $0.1 < M_{app}/M_M < 0.5$[45]]:

$$\theta_M = \alpha_\theta |M_{app}/M_M| \tag{4}$$

$$\phi_M = [\alpha_\phi |M_{app}/M_M| + \beta_\phi]\mathrm{sgn}(M_M), \tag{5}$$

where α_θ, α_ϕ, and β_ϕ are functions of k_H. Appendix A contains details of the linearization and interpolations of α_θ, α_ϕ, and β_ϕ as a function of k_H. Heuristically, θ_M is proportional to the perpendicular torque M_{app}, while ϕ_M is an odd roughly linear function of motor torque M_M, with a small dependence on M_{app}. We find that this model has $< 4\%$ error relative to the Kirchoff-rod calculation of (θ_M, ϕ_M) for the ranges $0 < 1/k_H < 3$ and $0 \le M_{app}/M_M \le 0.5$, corresponding to $0 \le \theta_M \le 55^\circ$ and $0 \le \phi_M \le 100^\circ$.

C. Calculation of swimming velocities, trajectories, and flagellum dynamics.

Using the linearized hook response and assuming a rigid flagellum, it is possible to efficiently calculate instantaneous swimming translational and rotational velocities, changes in flagellum orientation, and hence swimming trajectories and flagellum dynamics. In the low-Reynolds number limit appropriate to swimming bacteria[42], the translational and angular velocities of a rigid body are linearly related to the force and torque applied to the body. In our calculation, applied forces and torques are determined from the hook configuration, and then used to calculate the dynamics of connected cell body and flagellum. Given the flagellum orientation, the torque applied by the hook on the cell body is determined using the linearized model as

$$\mathbf{M}_c = M_M \hat{\mathbf{x}} + M_{app} \hat{\mathbf{n}}, \tag{6}$$

where $M_{app} = |M_M|\theta/\alpha_\theta$, and $\hat{\mathbf{n}}$ is the unit vector in the direction of $\hat{\mathbf{x}} \times \hat{\mathbf{r}}$ rotated by an angle $-\phi_M(M_{app}/M_M)$ about the x-axis. Then we calculate the velocity of the attachment point ($\mathbf{V}$) and the angular velocities of the cell body ($\mathbf{\Omega}_c$) and flagellum ($\mathbf{\Omega}_f$) about the attachment point as follows. By force and torque balance on the bacterium, the force and torque on the flagellum are $-\mathbf{F}_c$ and $-\mathbf{M}_c$, where $\mathbf{F}_c$ is the (unknown) force exerted by the hook on the cell body. We treat the hydrodynamics of the cell body and flagellum separately and ignore their hydrodynamic interactions, so

$$\begin{pmatrix} \mathbf{F}_c \\ \mathbf{M}_c \end{pmatrix} = \mathbf{R}_c \begin{pmatrix} \mathbf{V} \\ \mathbf{\Omega}_c \end{pmatrix}, \quad \begin{pmatrix} -\mathbf{F}_c \\ -\mathbf{M}_c \end{pmatrix} = \mathbf{R}_f \begin{pmatrix} \mathbf{V} \\ \mathbf{\Omega}_f \end{pmatrix}. \tag{7}$$

where $\mathbf{R}_c$ and $\mathbf{R}_f$ are the resistance matrices for the cell body and flagellum, calculated using our previously reported implementation[36–38] of the method of regularized Stokeslets[39, 40]. Equation 7 gives 12 linear equations which can be solved for the 12 unknown components of $\mathbf{V}$, $\mathbf{\Omega}_c$, $\mathbf{\Omega}_f$, and $\mathbf{F_c}$.

For an instantaneous orientation $\hat{\mathbf{r}}$ of the flagellum defined by (θ, ϕ), the swimming velocity $\mathbf{V}$, and body and flagellum angular velocities $(\mathbf{\Omega}_c, \mathbf{\Omega}_f)$ are found in the body coordinate system. The rate of change of flagellum orientation is specified by $(\dot{\theta}, \dot{\phi}, \dot{\gamma})$ (See Fig. 3a), which are obtained from the relative angular velocity $\mathbf{\Omega} = \mathbf{\Omega}_f - \mathbf{\Omega}_c$ and the geometric constraint $\dot{\hat{\mathbf{r}}} = \mathbf{\Omega} \times \hat{\mathbf{r}}$, as

$$\begin{aligned} \dot{\theta} &= \Omega_z \cos(\phi) - \Omega_y \sin(\phi), \\ \dot{\phi} &= \Omega_x - \cot(\theta)(\Omega_y \cos(\phi) + \Omega_z \sin(\phi)), \\ \dot{\gamma} &= \mathbf{\Omega_f} \cdot \hat{\mathbf{r}} \end{aligned} \tag{8}$$

where $\dot{\gamma}$ is the rotation rate of the flagellar filament along its centerline axis. We numerically integrate in time to obtain the trajectory of the flagellum orientation.

D. Extensible Kirchoff rod coupled to hydrodynamic forces.

To study how off-axis motion leads to bending of the flagellum, we must consider the deformations of a Kirchoff rod (representing the flagellum) under the influence of hydrodynamic forces. It is more convenient to couple external hydrodynamic forces into models of extensible, rather than inextensible Kirchoff rods[4, 23, 32, 35]. Flagella are neary inextensible, but in this model inextensibility is approximately enforced by adding a stiff extensional modulus that can be thought of as a penalty for filament extension.

We adopt the method used by Olson *et al* [4] to study the dynamics of an elastic rod interacting with an incompressible viscous fluid. Here, the filament represented by the Kirchoff rod is the flagellum, not the hook, so the curve $\mathbf{x}(s,t)$ describes the filament centerline of the flagellum, where $s \in [0, L]$ is a parameterization of the material arclength along the filament. As in the inextensible Kirchoff model, material frames are tracked by the orthonormal triad $\{\mathbf{d}_1(s,t), \mathbf{d}_2(s,t), \mathbf{d}_3(s,t)\}$. However, the inextensibility condition $|\partial_s \mathbf{x}(s,t)| = 1$ does not hold; in the undeformed state the unit vector $\mathbf{d}_3(s, t = 0)$

is equal to the tangent vector to the filament centerline ($\partial_s \mathbf{x}(s,t)$), but in general they are not equal.

Kirchoff rod theory relates the cross sectional force $\mathbf{F}(s,t)$ and moment $\mathbf{M}(s,t)$ to the external per unit length force $\mathbf{f}(s,t)$ and external per unit length moment $\mathbf{m}(s,t)$ applied by fluid on the filament,

$$0 = \partial_s \mathbf{F} + \mathbf{f} \tag{9}$$

$$0 = \partial_s \mathbf{M} + (\partial_s \mathbf{x} \times \mathbf{F}) + \mathbf{m}. \tag{10}$$

The constitutive relations for the extensible Kirchhoff rod are

$$\mathbf{F} = GA(\mathbf{d}_1 \cdot \partial_s \mathbf{x})\mathbf{d}_1 + GA(\mathbf{d}_2 \cdot \partial_s \mathbf{x})\mathbf{d}_2 + EA(\mathbf{d}_3 \cdot \partial_s \mathbf{x} - 1)\mathbf{d}_3 \tag{11}$$

$$\mathbf{M} = EI(\kappa_1 - \tau_1)\mathbf{d}_1 + EI\kappa_2 \mathbf{d}_2 + GJ(\kappa_3 - \tau_3)\mathbf{d}_3 \tag{12}$$

where EI and GJ are the bending and twist stiffnesses, respectively, while GA and EA allow extensibility of the rod. In the stiffnesses E and G are the Young's modulus and shear modulus, and A is the cross-sectional area of the filament. The values of GA and EA used in our calculations are listed in Table I, and taken from [4] and [35]. As for the inextensible rod, the twist vector $\boldsymbol{\kappa}(s,t)$ is related to the local material frames by $\partial_s \mathbf{d}_i = \boldsymbol{\kappa} \times \mathbf{d}_i$. The initial shape of the flagellar filament is set to be a tapered helix with centerline described in the SM, and τ_1 and τ_3 are reference curvatures chosen so that in the initial configuration $\mathbf{M} = 0$.

Given a current configuration of the filament $\mathbf{x}(s)$, the time evolution of $\mathbf{x}(s,t)$ and $\mathbf{d}_i(s,t)$ is numerically obtained by using Eqs. 9-12 to determine the hydrodynamic force $\mathbf{f}$ and moment $\mathbf{m}$ on discretized segments of the filament. Since hydrodynamic forces and torques on the filament are equal and opposite to the forces and torques applied by the filament on the fluid, we can use the forces and torques in the method of regularized Stokeslets to calculate the fluid flow fields everywhere, and hence by the no slip boundary condition the translational and rotational velocities of filament segments. Time integration of the velocities yields the configuration of the filament as a function of time. Details of our numerical implementation are in Appendix B. For our choices of stiffness parameters and motions, the arclength changes by at most 0.2% so the flagellum remains nearly inextensible.

III. RESULTS

A. Flagellar orbits and precession.

Linearizing the hook makes calculation of the time-dependent swimming behavior of a bacterium with a flexible hook but rigid cell body and rigid flagellum significantly less computationally expensive, allowing investigation of a wide enough range of body geometries and hook stiffnesses to connect to experiments. In this and the next section the cell body is an ellipsoid with the mean geometry listed in Table I, and the same flagellum geometry as above. Neglecting the hook length, the flagellum is attached at the pole of the cell body and instantaneously oriented along $\hat{\mathbf{r}} = \cos(\theta)\hat{\mathbf{x}} + \sin(\theta)\cos(\phi)\hat{\mathbf{y}} + \sin(\theta)\sin(\phi)\hat{\mathbf{z}}$. A constant negative motor torque M_M is applied to give CCW rotation. We compute the trajectory of flagellum orientation (θ, ϕ) during swimming. If the helical centerline of the flagellum is initially oriented in the x-direction, after a transient it moves around a central direction $\mathbf{r}^*$ [at (θ^*, ϕ^*)] such that the end point of the centerline nearly traces a circle (dashed circle in Fig. 3a, example trajectories in Fig. 3b,c).

For stiff hooks ($k_H > k_H^* \approx 0.552$), a stable orbit around $\mathbf{r}^*$ occurs for each motor revolution and the deflection angle $\Delta\theta$ between the flagellum orientation $\mathbf{r}$ and $\mathbf{r}^*$ is small. In Fig. 3b we show a typical trajectory of the flagellum orientation in this regime. Initially the flagellum is in the x-direction, but after a transient stabilizes in a nearly circular trajectory. The deflection angle of the hook is quite small throughout. Stable orbits were identified by direct time evolution. Orbits can also be identified as the fixed points (modulo 2π) of the discrete map

$$\mathcal{F} : (\theta_i, \phi_i) \mapsto (\theta_i + \int_0^{2\pi} \theta' \, d\gamma, \phi_i + \int_0^{2\pi} \phi' \, d\gamma) = (\theta_f, \phi_f), \tag{13}$$

where $(\theta', \phi') = (d\theta/d\gamma, d\phi/d\gamma) = (\dot{\theta}/\dot{\gamma}, \dot{\phi}/\dot{\gamma})$. Stability of an orbit was evaluated by constructing a Poincare map on a local line in (θ, ϕ) space transverse to the orbit: if ζ is a coordinate along the line such that $\zeta = 0$ is on the orbit, the Poincare map takes ζ_n to $\zeta_{n+1} = g(\zeta_n)$, which is the next intersection of the orientation trajectory with the line. Linearizing around $\zeta = 0$, $g(\zeta) \approx \tilde{g}\zeta$, and orbits are asymptotically stable if $|\tilde{g}| < 1$. Stable orbits identified using this metric matched stable orbits identified by direct time evolution of the dynamics.

For less stiff hooks or greater motor torques ($k_H < k_H^*$), orbits become unstable and instead the flagellum precesses, taking multiple flagellar revolutions to circle around $\mathbf{r}^*$. During precession, typical deflection angles $\Delta\theta$ are much larger than during orbits. In Fig. 3c we show a typical orientation trajectory in this regime. After a transient, the precessional behavior can be seen in which $\hat{\mathbf{r}}$ wiggles as it traces out the circle, staying between two angles θ^{min} and θ^{max} as it precesses. Each small loop in the transient or wiggle in the outer precessional circle corresponds to a single motor revolution. Because the precession angle is large, the transient takes many (≈ 20) motor revolutions. Fig. 3d shows how $\Delta\theta$ and the radius of the circle traced by the flagellum endpoint increase as k_H decreases and orbits transition to precession.

For both orbiting and precession, the center of the orbit or precession remains quite close ($\theta^* < 0.01°$) to the x-axis for all values of k_H investigated.

Our results are consistent with the precession-like behavior robustly observed across a variety of systems with flexible hooks and rigid flagella. Ref [30] found orbits

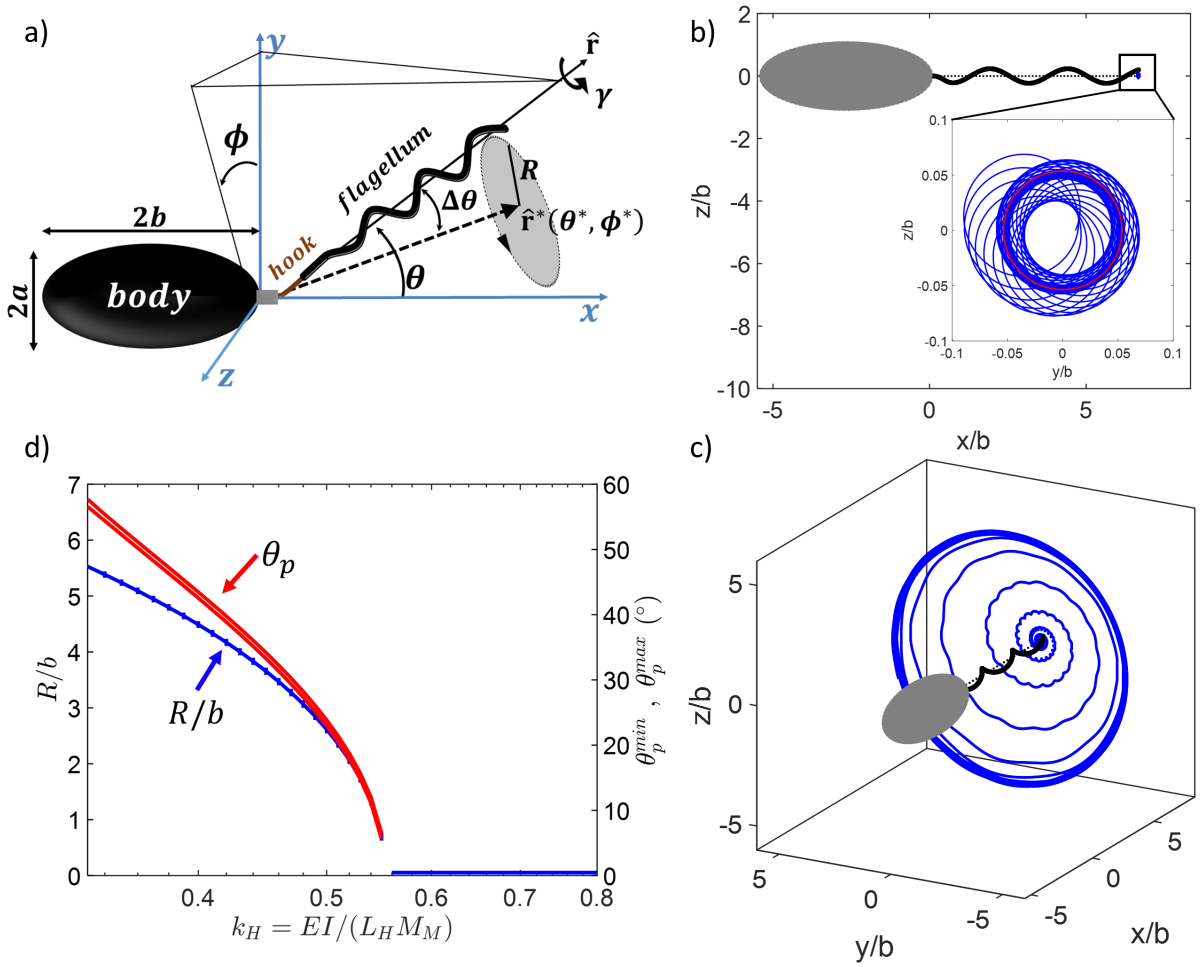

FIG. 3. a) Orientation of flagellum along $\hat{\mathbf{r}}$ described by angles (θ,ϕ) traces a nearly-circular trajectory (dashed line) around average orientation $\hat{\mathbf{r}}^*$. b,c) Examples of the flagellar orientation trajectories during free swimming with linearized hook dynamics. The flagellum is initially oriented in the x-direction and after a transient motion the settles into either orbits or precession. The blue trace is the motion of the flagellum endpoint relative to the cell body for motor moment of $M_M = 2000$ pN nm. For $k_H = 1 > k_H^*$ (b) the long-time motion is a small orbit, shown as a red circle. One orbit traversal takes one flagellar rotation. For $k_H = 0.36 < k_H^*$ (c) the long-time motion is precession closely following the largest circular paths. One traversal around the path takes multiple flagellar rotations. d) Trajectory size measured by minimum (θ_p^{min}) and maximum (θ_p^{max}) deflection angles (red lines) or radius of end-point motion (R, blue line). In model with rigid flagellum, as stiffness parameter k_H decreases flagellum trajectories transition from small orbits to large precession at k_H^*.

which became unstable as hooks became less stiff, and precession was observed and modeled[33] for bacteria stuck to a slide. However, precession itself can not explain flick initiation; for a simple torsional spring[31] as well as in our more realistic linearization, precession would lead to helical swimming trajectories[31], not flicks. Even supposing that the flick is just a portion of a helical trajectory lasting until hook stiffness increases, experimental movies[29] show $\approx 90°$ flagellar deflection during flicks, while in our model we find θ significantly less than 60° for a wide range of $k_H < k_H^*$.

B. Flicks require flagellar bending.

Buckling of the hook alone leads to precession and helical trajectories with too small deflection angles to explain flicks. In the above, the flagellum was assumed to be rigid, but large precessional rotations introduce significant forces on the flagellum which may cause it to bend. Bending of both the flagellum and hook is thus essential for understanding flicks. To determine whether precessional orbits lead to the bending observed in flicks, we prescribe that the base of the flagellum translates and rotates its orientation exactly as predicted by the rigid model above, and ignore the hydrodynamic interactions with the cell body and hook. The flexible flagellum is started with the same configuration as a rigid

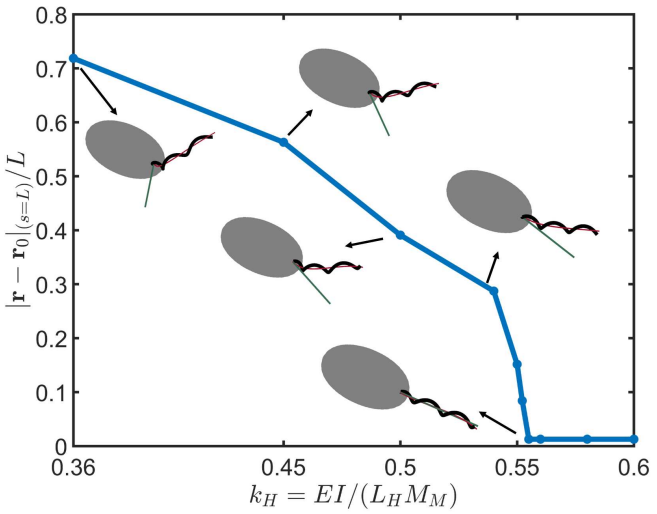

FIG. 4. Adding flagellum flexibility, for $k_H > k_H^*$ flagellum remains nearly unbent and on-axis, while for $k_H < k_H^*$ stresses from precession lead to large deformations from rigid flagellum (straight grey line), as measured by endpoint displacement between bent and rigid flagellum $|\mathbf{r}-\mathbf{r}_0|_{(s=L)}$.

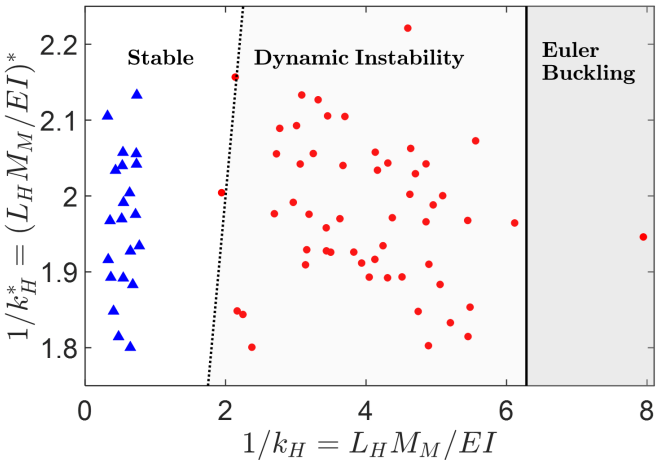

FIG. 5. Calculated $1/k_H$ values of post-flick (blue triangles) runs lie in the stable regime to the left of the critical value (dashed line) predicted by the dynamic buckling instability, while those of pre-flick runs (red circles) lie in the unstable regime. Nearly all pre-flick runs do not exceed the static Euler buckling criterion (solid line).

flagellum then allowed to evolve in time. If the model shows little flagellar bending the rigid flagellum assumption is valid and precessional orbits are predicted, but if it shows significant flagellar bending, the actual (uncalculated) dynamics will be strongly affected by both hook and flagellum bending. We use this approach rather than directly simulating the full swimming dynamics incorporating hook and flagellum flexibility since the extensible Kirchoff rod model is computationally expensive, and due to long transients we could not reliably identify long-time flagellar behavior under full swimming dynamics.

Movies S1-5 show the resulting flexible flagellar motion for k_H above and below the critical value, along with fits of the deformed centerline of the flagellum (red line) and, for comparison, the location of the rigid flagellum. For orbits with small $\Delta\theta$ ($k_H > k_H^*$), deflections of the flexible flagellum are small. On the other hand, for precessional motion ($k_H < k_H^*$), flagellar deflections are large. We quantify deflections via the displacement between the endpoint of the deformed centerline and the rigid centerline at a time corresponding to half of a precessional rotation (Fig. 4). The bending displacement is significant even for $k_H = 0.55$, nearly immediately below k_H^*. Thus after accounting for flagellum flexibility, for $k_H < k_H^*$ precession is not observed; instead significant flagellar bending alters the dynamics. Thus, together with hook bending, the flagellar bending apparent in movies of flicks[29] is necessary for flick initiation.

By comparison, the only previous simulations of flicks[32] choose flagellar stiffness such that the flagellum hardly bends, and find deflections of at most 25°. These simulations do not quantitatively predict the critical stiffness for the onset of flicks, possibly since the flagellum base is fixed in position rather than free-swimming, or since the spatial resolution of short hooks was limited.

C. Comparison to experiments and discussion.

The results above imply that flicks are initiated by the dynamic buckling instability when $k_H = EI/M_M L_H < k_H^*$. The critical k_H^* depends on body and flagellum geometry. To compare with experimentally observed runs (Table S1) we calculate k_H^* for the body geometry of each run, and in Fig. 5 plot $1/k_H^*$ against $1/k_H = M_M L_H/EI$ obtained from the regularized Stokeslet calculation of the torque, $L_H = 100$nm, EI_u for pre-flick runs, and EI_w for post-flick runs. The dotted line is $1/k_H^* = 1/k_H$, so stable orbits are predicted to the left and above the dotted line, while dynamical buckling is predicted to the right and below, in good agreement with the distribution of post- and pre-flick runs. Notably, only one pre-flick run exceeds the Euler buckling condition (solid line)[46] in addition to our dynamic instability condition. Fig. 5 strongly supports the claim that flicks are initiated by the dynamic instability of the hook and flagellum that we have identified rather than static Euler buckling of the hook. Although our models and the experiments are specific to *Vibrio alginolyticus*, we expect that the physical conclusions arising from flexible filaments are robust. In particular, as torque increases, our dynamical transition occurs before the static Euler buckling condition is met, especially since as noted above the orbit-precession transition for hook-mediated rotation is robust across models.

Our calculations ignored displacement of the hook endpoint and hydrodynamic interactions between the flagellum, hook, and cell body, which we expect to result in 15-20% errors, in the same range as the uncertainty of the measured EI_u. We have not calculated the full swim-

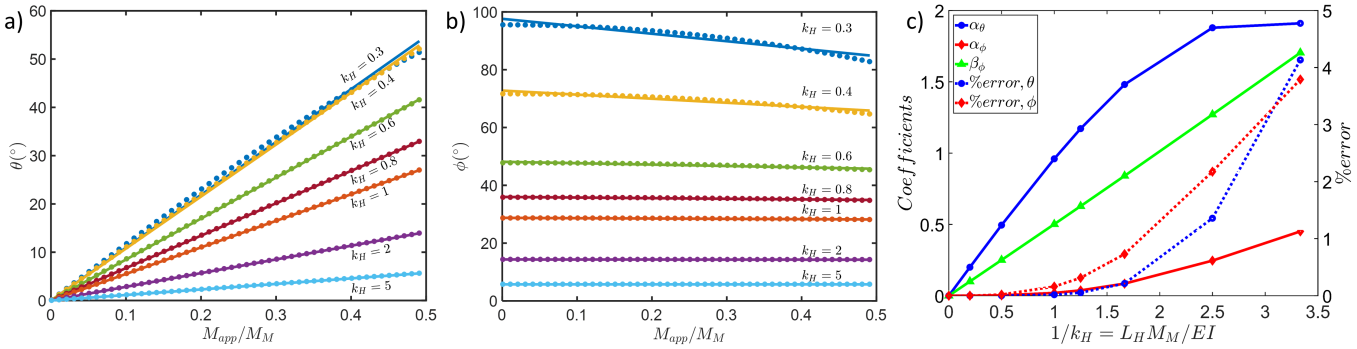

FIG. 6. The linear response of hook deflection angles to applied moments. a,b) Dots are the response of deflection angles (θ, ϕ) for the exact Kirchhoff rod model, while lines are the linear interpolations for different relative stiffnesses k_H. The coefficients plotted in c) are the intercepts and slopes of these linear interpolations. c) The linearization coefficients for the orientation angles (θ, ϕ) and associated errors. The corresponding relations are Eq. 4 and 5.

ming and bending dynamics during the flick, only determined the mechanism of flick initiation. To model the full kinematics of a flick requires knowledge of the time- and winding-dependent stiffness of the hook and treating a fully flexible flagellum and hook for a swimming bacterium with full hydrodynamic interactions, which is computationally expensive if one wished to model multiple cell body geometries. For hook deflections within its range of validity, our linearized model could aid in this goal, especially since other models of flexible hooks and flagella may be limited by insufficient resolution of the hook[32], which is an order of magnitude shorter than the flagellum. Our results indicate that dynamical instabilities must be accounted for in designs incorporating slender filaments since they can occur before static failure, although we expect any instabilities to be highly dependent on details of system geometries and actuation.

Appendix A: Details for linearization of hook

As described in Section II B, we apply a motor torque (M_M) in x-direction and a torque M_{app} in z-direction, and calculate the orientation at the end point $[\mathbf{d_3}(s = L_H)]$ expressed in terms of the polar coordinates (θ, ϕ) (see Fig. 2). The results calculated for $M_M = 2000$ pN nm and $L_H = 100$ nm are shown in Fig. 6. We vary EI to select a fixed value of $k_H = EI/M_M L_H$, then plot the angles (θ, ϕ) as a function of varying M_{app}. It is evident that θ is nearly linear in M_{app} and ϕ has only a slight dependence on M_{app} in the investigated range. For each k_H, we perform a linear fit of the angle as a function of M_{app}/M_M, then numerically interpolate those as a function of k_H to find the linear fit reported in the main text with coefficients

$$\begin{aligned}
\alpha_\theta &= 0.0024/k_H^4 - 0.05/k_H^3 + 0.013/k_H^2 + 1/k_H, \\
\alpha_\phi &= 0.05/k_H^2 - 0.031/k_H \\
\beta_\phi &= 0.5/k_H. \qquad \text{(A1)}
\end{aligned}$$

Fig. 6c shows the coefficients and percent error in the fits as a function of $1/k_H$. By comparing this range $(0 \leq M_{app}/M_M \leq 0.5)$ to those in Fig. 6a,b, one can see that the linear fits have less than 5% error as long as $\theta < 55^\circ$ and $\phi < 100^\circ$. Finally, we repeated the procedure for motor torques $M_M = \{500, 1000, 4000, 6000\}$ pN nm and found that the coefficients have the same dependence on k_H for all the motor torques.

In the above, the force $\mathbf{F}_0 = 0$. To investigate the effect of $\mathbf{F}_0$ on the orientation of the end point, we considered the case with $M_M = 2000$ pN nm and $M_{app}/M_M = 0.5$, typical values for the torque. Since a typical force magnitude due to flagellar propulsion is 1 pN, to be conservative we applied a force with $(F_{0,x}, F_{0,z}) = (1, 0.8)$ pN. The latter value correponds to the z-component of flagellar force when the deflection angle $\theta = 55^\circ$. The results are plotted for varying stiffnesses in Fig. 7. The error due to ignoring the contribution of force to the deflection angles is always less than 4%. Finally, we also measure the magnitude of the displacement of the hook at the end of the hook $(s = L_H)$, and find that for typical forces and torques the end of the hook can be displaced by up to about $0.5L_H$. While this is a large fraction of the hook length, in the context of the bacterium it only amounts to 50 nm, which is an order of magnitude smaller than the length of the flagellum; hence we ignore the effects of hook displacements for bacterial dynamics.

Appendix B: Numerical implementation of extensible Kirchoff rod

We couple the extensible Kirchhoff rod model (Eqs. 9-12) with hydrodynamic forces calculated by using surface distributions of regularized Stokeslets [39]. We uniformly discretize the centerline of the filament along the arc length into N segment of length Δs. There are $N+1$ cross sections at points $s_p = p\Delta s$, for $p = 0, 1, .., N+1$. The center of segment p is at the half-integer-indexed point $s_{p+1/2}$. We represent each segment as a cylinder under-

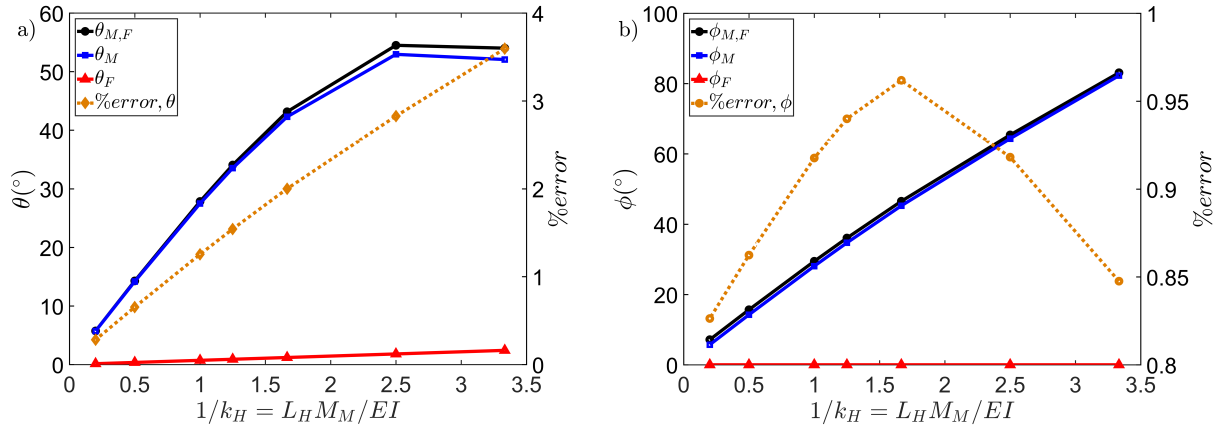

FIG. 7. The effects of applied force on the deflection angles. a) $\theta_{M,F}$ is the deflection angle due to applying a typical moment and upper bound for the force, while θ_M and θ_F are the deflection angles when applying only the moment or force, respectively. The dashed line represents percentage change in the deflection due to the force compared to due the moment. b) Similar quantities for the torsional deflection ϕ due to applied moment and force.

going rigid body dynamics, and uniformly discretize the surface of each cylinder using N_s regularized Stokeslets as shown in Fig. 8. Note that since the segment has finite extent, torques can result from the force distribution on the segment and there is no need to include rotlet singularities.

The position of each segment of the filament determines the position $\mathbf{x}(s_{p+1/2})$, and the orientation of each segment determines the frame $\mathbf{d}_i(s_{p+1/2})$ at each center point $p+1/2$. The discretized versions of the Kirchoff equations for force and moment balance (Eq. 9 and 10) for segment $p+1/2$ are

$$0 = \mathbf{F}_{p+1} - \mathbf{F}_p + \sum\nolimits_i \mathbf{f_i} \tag{B1}$$

$$0 = \mathbf{M}_{p+1} - \mathbf{M}_p + 0.5[(\partial_s \mathbf{x} \times \mathbf{F})_{p+1} - (\partial_s \mathbf{x} \times \mathbf{F})_p] + \sum\nolimits_i (\mathbf{r}_i - \mathbf{x}(s_{p+1/2}, t)) \times \mathbf{f_i} \tag{B2}$$

where $\sum_i \mathbf{f_i}$ is the total force from regularized Stokeslets on surface of the segment (i.e., the force from the interaction of a rigid segment and the fluid), $\mathbf{r}_i$ is the position vector of the points on the surface of the segment, and $(\partial_s \mathbf{x})_p = [\mathbf{x}(s_{p+1/2}) - \mathbf{x}(s_{p-1/2})]/\Delta s$. Given the current configuration, Eqs. 11 and 12 determine $(\mathbf{F}_p, \mathbf{M}_p)$, hence B1 and B2 determine the total hydrodynamic force $(\sum_i \mathbf{f_i})$ and torque $(\sum_i (\mathbf{r}_i - \mathbf{x}(s_{p+1/2}, t)) \times \mathbf{f_i})$ on each segment, which acts as a constraint on each segment. In Eqs. 11, and 12, the frame $\mathbf{d}_i(s_p)$ is interpolated between $\mathbf{d}_i(s_{p-1/2})$ and $\mathbf{d}_i(s_{p+1/2})$) [35]. Assuming rigid body motion of each segment, the method of regularized Stokeslets is then used to find translational and angular velocities $(\mathbf{u}_{p+1/2}, \mathbf{\Omega}_{p+1/2})$ of each segment that satisfy the force and torque constraints and no-slip boundary conditions on all surfaces. This is accomplished using the same method as for swimming bacterium in [37], except here each segment has a separate force constraint, instead of just the flagellum and cell body having separate force constraints. From these velocities we compute

$$\partial_t \mathbf{x}(s_{p+1/2}) = \mathbf{u}_{p+1/2} \tag{B3}$$

$$\partial_t \mathbf{d}_i(s_{p+1/2}) = \mathbf{\Omega}_{p+1/2} \times \mathbf{d}_i(s_{p+1/2}) \tag{B4}$$

at each time step and numerically integrate in time to evolve the shape of the flexible flagellum.

ACKNOWLEDGMENTS

We thank K. Son, J. Guasto, and R. Stocker for sharing and allowing us to publish the original data from [29]. This work was supported by National Science Foundation award CBET-1651031 to HCF.

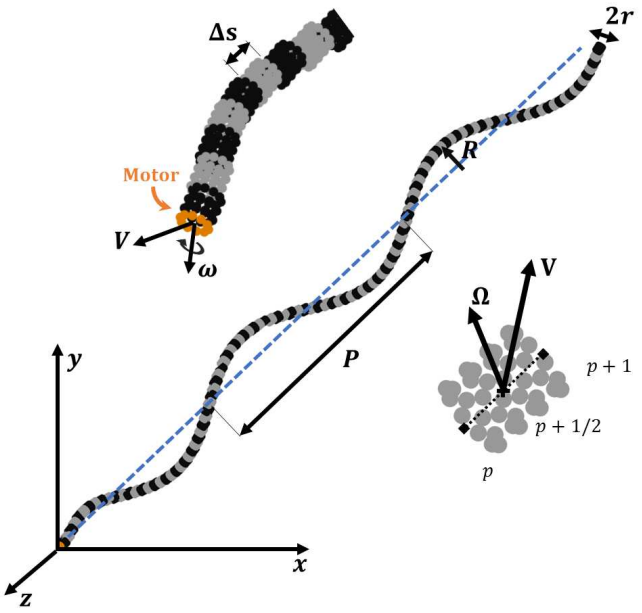

FIG. 8. The regularized Stokeslet method is coupled with an extensible Kirchhoff rod model to model a flexible flagellum. The flagellum is discretized into cylindrical segments of length Δs. Cross sections between the segments are labeled by integers p, while segment centers are labeled by half-integers $p + 1/2$. Each segment is treated as a rigid body with translational and angular velocities $\mathbf{V}$ and Ω. The elastic forces from deformation are calculated from the relative motion of segments. Points show regularized Stokeslets on the surface of each segments. A prescribed velocity and rotation rate is applied to the cell end of the flagellum ($s = 0$) and then the time-dependent deflections of the flagellum are calculated.

[1] C. H. Wiggins and R. E. Goldstein, Physical Review Letters **80**, 3879 (1998).
[2] C. W. Wolgemuth, T. R. Powers, and R. E. Goldstein, Physical Review Letters **84**, 1623 (2000).
[3] B. Qian, T. R. Powers, and K. S. Breuer, Physical Review Letters **100**, 078101 (2008).
[4] S. D. Olson, S. Lim, and R. Cortez, Journal of Computational Physics **238**, 169 (2013).
[5] M. Jawed, N. Khouri, F. Da, E. Grinspun, and P. Reis, Physical Review Letters **115**, 168101 (2015).
[6] M. Jawed and P. Reis, Physical Review Fluids **2**, 034101 (2017).
[7] Y. Takano and T. Goto, JSME International Journal Series C Mechanical Systems, Machine Elements and Manufacturing **46**, 1234 (2003).
[8] H. Hoshikawa, Biophysical Chemistry **17**, 105 (1983).
[9] H. Hoshikawa and R. Kamiya, Biophysical Chemistry **22**, 159 (1985).
[10] M. Kim and T. R. Powers, Physical Review E **71**, 021914 (2005).
[11] N. C. Darnton and H. C. Berg, Biophysical Journal **92**, 2230 (2007).
[12] M. K. Jawed and P. M. Reis, Soft Matter **12**, 1898 (2016).
[13] Y. Takano, K. Yoshida, S. Kudo, M. Nishitoba, and Y. Magariyama, JSME International Journal Series C Mechanical Systems, Machine Elements and Manufacturing **46**, 1241 (2003).
[14] T. C. Adhyapak and H. Stark, Soft Matter **12**, 5621 (2016).
[15] R. Vogel and H. Stark, The European Physical Journal E: Soft Matter and Biological Physics **35**, 1 (2012).
[16] S. Trachtenberg and I. Hammel, Journal of Structural Biology **109**, 18 (1992).
[17] T. C. Flynn and J. Ma, Biophysical Journal **86**, 3204 (2004).
[18] M. Kim, J. C. Bird, A. J. Van Parys, K. S. Breuer, and T. R. Powers, Proceedings of the National Academy of Sciences **100**, 15481 (2003).
[19] H. Flores, E. Lobaton, S. Méndez-Diez, S. Tlupova, and R. Cortez, Bulletin of Mathematical Biology **67**, 137 (2005).
[20] N. Watari and R. G. Larson, Biophysical Journal **98**, 12 (2010).
[21] P. Janssen and M. Graham, Physical Review E **84**, 011910 (2011).
[22] S. Y. Reigh, R. G. Winkler, and G. Gompper, PLoS One **8**, e70868 (2013).
[23] S. Lim and C. S. Peskin, Physical Review E **85**, 036307 (2012).
[24] T. C. Adhyapak and H. Stark, Physical Review E **92**, 052701 (2015).
[25] M. J. Kühn, F. K. Schmidt, B. Eckhardt, and K. M. Thormann, Proceedings of the National Academy of Sciences **114**, 6340 (2017).
[26] M. Manghi, X. Schlagberger, and R. R. Netz, Physical Review Letters **96**, 068101 (2006).
[27] N. Coq, O. Du Roure, J. Marthelot, D. Bartolo, and M. Fermigier, Physics of Fluids **20**, 051703 (2008).
[28] L. Xie, T. Altindal, S. Chattopadhyay, and X.-L. Wu, Proceedings of the National Academy of Sciences **108**, 2246 (2011).
[29] K. Son, J. S. Guasto, and R. Stocker, Nature Physics **9**, 494 (2013).
[30] H. Shum and E. Gaffney, Physics of Fluids **24**, 061901 (2012).
[31] F. T. Nguyen and M. D. Graham, Biophysical Journal **112**, 1010 (2017).
[32] Y. Park, Y. Kim, W. Ko, and S. Lim, Physical Review E **95**, 022410 (2017).
[33] Y. Shimogonya, Y. Sawano, H. Wakebe, Y. Inoue, A. Ishijima, and T. Ishikawa, Scientific Reports **5**, 18488 (2015).
[34] The data were originally taken and analyzed in Ref. [29] using the methods described therein. In [29] only the 1D model estimates of force and torque were reported; Table S1 has previously unpublished data of cell body geometries and swimming speeds for each imaged run.
[35] S. Lim, A. Ferent, X. S. Wang, and C. S. Peskin, SIAM Journal on Scientific Computing **31**, 273 (2008).
[36] Y. Hyon, T. R. Powers, R. Stocker, H. C. Fu, *et al.*, Journal of Fluid Mechanics **705**, 58 (2012).
[37] J. Martindale, M. Jabbarzadeh, and H. Fu, Physics of Fluids **28**, 021901 (2016).
[38] M. A. Constantino, M. Jabbarzadeh, H. C. Fu, and R. Bansil, Science Advances **2**, e1601661 (2016).
[39] R. Cortez, SIAM Journal on Scientific Computing **23**, 1204 (2001).
[40] R. Cortez, L. Fauci, and A. Medovikov, Physics of Fluids **17**, 031504 (2005).
[41] See Supplemental Material at [URL will be inserted by publisher] for details of flagellum geometry.
[42] E. M. Purcell, American Journal of Physics **45**, 3 (1977).
[43] H. C. Berg, Annual Review of Biochemistry **72** (2003).
[44] Y. Sowa, H. Hotta, M. Homma, and A. Ishijima, Journal of Molecular Biology **327**, 1043 (2003).
[45] The range of M_{app} is obtained from the hydrodynamic model of swimming used for Fig. 1.
[46] Calculated assuming a typical axial force $F = 0.83$ pN and EI_u.